Supplementary Information (SI) for Journal of Materials Chemistry C.

Supporting Information

Dual-Functionality of Phosphorescence and Photothermal Conversion through Light-Activated Open-Shell Singlet Diradicals in Silver Metal-Organic Frameworks

*Pei-Yu Liao,† Jia-Chuan Liu,† Hao-Zhi Fan, Yi Ding and Ming-Liang Tong**

Key Laboratory of Bioinorganic and Synthetic Chemistry of Ministry of Education, School of Chemistry, IGCME, GBRCE for Functional Molecular Engineering, Sun Yat-Sen University, Guangzhou 510006, P. R. China

**E-mail: tongml@mail.sysu.edu.cn*

Table of Contents

1 Experimental Procedures

1.1 Materials and General Procedure.

All chemicals were purchased from commercial sources and used as received without further purification. The C, H, N elemental analyses were carried out with an Elementar Vario-EL Cube CHNS elemental analyzer. Attenuated total reflectance (ATR) infrared spectra (500−4000 cm^{-1} region) were measured at room temperature with the PerkinElmer Frontier infrared spectrometer. Thermogravimetric analysis (TGA) was carried out on a TG-209F1 Libra thermogravimetric analyze under N_2 atmosphere. Powder X-ray diffraction (PXRD) patterns were performed on a Rigaku Smartlab X-Ray Diffratometer with Cu-$K\alpha$ (λ = 1.54178 Å) radiation. The powder diffraction simulation patterns were simulated using Mercury program based on single-crystal crystallographic data. UV-Vis-NIR spectra were measured at room temperature on a Shimadzu UV-3600Plus UV-Vis-NIR spectrophotometer equipped with an integrating sphere attachment. $BaSO_4$ was used as a reference. Illumination experiments were conducted using an LED UV lamp (365 nm; 27 W). Meanwhile, 15 mg of the original samples were uniformly dispersed in approximately 400 mg of $BaSO_4$ for the measurement of UV-Vis-NIR diffuse reflectance spectra.

1.2 Single-Crystal X-ray Crystallography.

Single-crystal X-ray diffraction (SC-XRD) measurements were performed on a Bruker D8 QUEST diffractometer with Mo-$K\alpha$ (λ = 0.71073 Å) radiation at 120.00 K. The Data indexing and integration were carried out with Bruker APEX-IV software. The structures were solved by direct methods using SHELXTL[1] and Olex2[2] program packages. All non-hydrogen atoms were refined with anisotropic displacement parameters by least-squares technique on weighted F^2 values.[3] Hydrogen atoms were added geometrically and refined using the riding model. The solvents in the lattice of **1** was highly disordered and were squeezed using the solvent mask function in Olex2.[4] Crystallographic data (CCDC No. 2415265) can be obtained for free from the Cambridge Crystallographic Data Centre via https://www.ccdc.cam.ac.uk/structures/.

1.3 Photoluminescence Measurements.

Steady-state/transient-state photoluminescence spectra were measured on an Edinburgh FLS-1000 Fluorescence spectrometer equipped with a visible photomultiplier tube (PMT) and an NIR PMT. Excitation was performed using a continuous Xenon lamp. All the excitation and emission spectra were corrected for the instrumental functions. Decay data were collected by using external excitation light sources. The fluorescence lifetimes at the nanosecond scale were measured by a picosecond pulsed laser at 405 nm (HPL 405), and the phosphorescence lifetimes were measured by a microsecond flash at 355 nm. The variable temperature process made use of the liquid nitrogen for cooling. Each sample was measured several times under comparable experimental conditions.

1.4 Electron Paramagnetic Resonance Analysis

A Bruker ESR5000 instrument in the X-band with microwave frequency of 9463.3 MHz was used for EPR measurements. Variable temperature ESR texts were carried out under the same instrument equipped with variable temperature accessories, and the external coolant is liquid nitrogen. The temperature of target MOF **1** and **1*** powders changed from 100 K to 300 K.

1.5 Near-infrared Photothermal Conversion.

MOF **1** and **1*** powder samples (10 mg, respectively) were pressed into thin disks with a diameter of 4 mm and placed under the 808 nm laser lamp (RAL808T1, Ra-laser, Beijing, China). The power density of the laser was adjusted between 0.1 and 1.0 W cm^{-2} and was confirmed by a photometer (CEL-NP2000-2A, Au-light, Beijing, China). The measurements conducted on different samples were both under the same conditions. An IR thermal camera (Fotric 246M ,Fotric, Shanghai, China) was used to capture the infrared videos of the MOFs samples when the illumination was on/off. The infrared photos and real-time temperatures were extracted from the video by AnalyzIR software. The solar-driven water evaporation was carried out using a 500 W Xenon lamp (CEL-S500-T5) equipped with an AM 1.5 G optical filter.

1.6 Computational Details.

The (U)B3LYP functional and def2-svp basis sets were employed in this article to perform all the (TD-)DFT calculations. DFT-D3 correction[5] was taken into account. The structures used in all the calculations were derived from SC-XRD data of complex **1**. The Gaussian package[6] was used for all of our calculations. Multiwfn software[7] was used to analyze wavefunction data produced by Gaussian. Visual molecular dynamics software[8] was used to visualize calculation results. The structural motif $\{Ag(TEPE)_4\}^+$ was chosen as a simple model for the perceived photo-active component of the MOF material.

1.7 Synthesis of [Ag(TEPE)](ADC)·9H$_2$O (1).

The mixture of Ag_2O (0.05 mmol), 1-adamantane carboxylic acid (ADCA, 0.05 mmol) and 1,1,2,2-tetra(pyridin-4-yl)ethene (TEPE, 0.05 mmol) was dissolved in 5 mL MeOH and stirred for 5 minutes. Subsequently, 0.5 mL 25% $NH_3 \cdot H_2O$ was added dropwise to the suspension and stirred for an additional 1 hour until the solution became clear. The filtration was left for several days to obtain light-yellow crystals of **1** (Yield: 0.023 g, 29.3% based on Ag). Elemental analysis calcd. (%) for $C_{33}H_{49}AgN_4O_{11}$; C: 50.45, H: 6.29, N: 7.13; found (%): C: 50.52, H: 6.12, N: 7.07. IR (ATR, cm^{-1}): 3395 (br), 3055 (br), 2900 (vs), 2847 (w), 1597 (s), 1539 (vs), 1450 (w), 1414 (s), 1384 (vs), 1307 (s), 1248 (w), 1218 (vs), 1069 (s), 1009 (w), 885 (s), 825 (w), 795 (vs), 754 (w), 682 (w), 630 (s), 575 (s).

2. Results and Discussion

2.1 Experimental Procedures

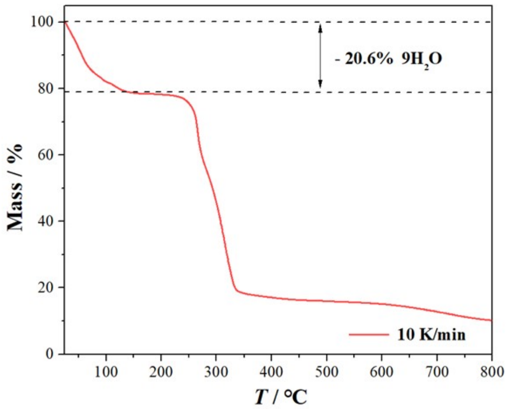

Figure S1. Thermogravimetric analysis for **1** under N_2 atmosphere (10 K min^{-1}). The dashed lines correspond to the theoretical weight loss percentage of 9 H_2O.

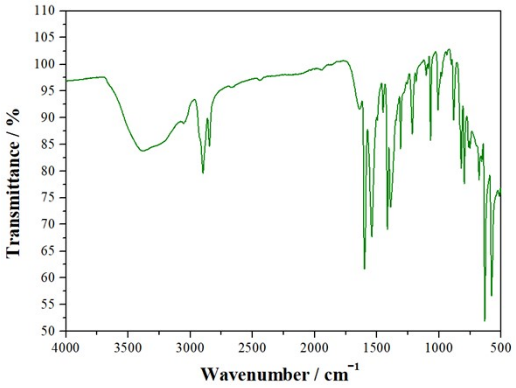

Figure S2. IR spectra of **1**.

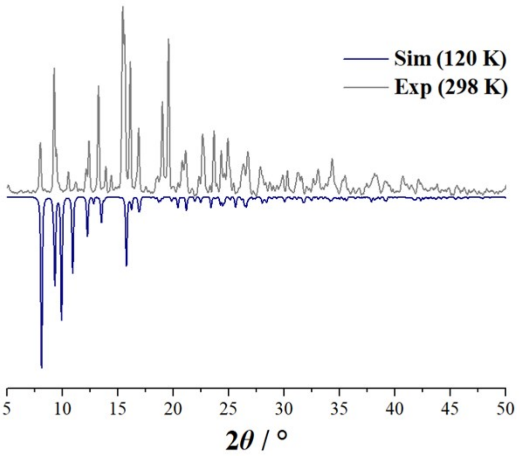

Figure S3. The PXRD pattern for **1** (grey line) at room temperature. The simulated pattern (blue line) based on the single crystal structure is shown for comparison.

2.2 Crystallographic Data and Structures

Table S1. Crystallographic data and structural refinements for **1**.

Compound	**1**
Formula	$C_{33}H_{49}AgN_4O_{11}$
Formula weight	785.63
Temperature / K	120.00
Crystal system	orthorhombic
Space group	$Pcca$
a / Å	17.9061(13)
b / Å	19.3385(15)
c / Å	21.8682(16)
α / °	90
β / °	90
γ / °	90
V / Å^3	7572.5(10)
Z	8
$\rho_{calcd.}$ / g/cm^{-3}	1.378
μ / mm^{-1}	0.592
F000	3280.0
Reflections collected	77995
Independent reflections	8671 [$R_{\text{int}} = 0.0558$, $R_{\text{sigma}} = 0.0397$]
GOF on F^2	1.113
R_1, wR_2 [$I \geq 2\sigma(I)$]^a	$R_1 = 0.0714$, $wR_2 = 0.2040$
R_1, wR_2 (all data)	$R_1 = 0.0905$, $wR_2 = 0.2169$
Largest diff. peak/ hole / e Å^{-3}	1.30/−0.69
CCDC No.	2415265

$^aR_1 = \sum||F_o| - |F_c||/\sum|F_o|$. $wR_2 = [\sum w(F_o^2 - F_c^2)^2/\sum w(F_o^2)^2]^{1/2}$.

Table S2. Selected bond lengths (Å) and angles (°) for **1**.

Bond lengths (Å)			
Ag1−N1	2.314(4)	Ag1−N3^A	2.399(5)
Ag1−N2	2.268(4)	Ag1−N4^B	2.291(4)
Bond angles (°)			
N1−Ag1−N3^A	84.84(18)	N2−Ag1−N4^B	116.06(15)
N1−Ag1−N2	118.55(17)	N4^B−Ag1−N1	111.71(15)
N2−Ag1−N3^A	114.61(16)	N4^B−Ag1−N3^A	106.49(17)

Symmetry codes: (A) 1/2-X,1-Y,+Z; (B) 1/2-X,+Y,-1/2+Z

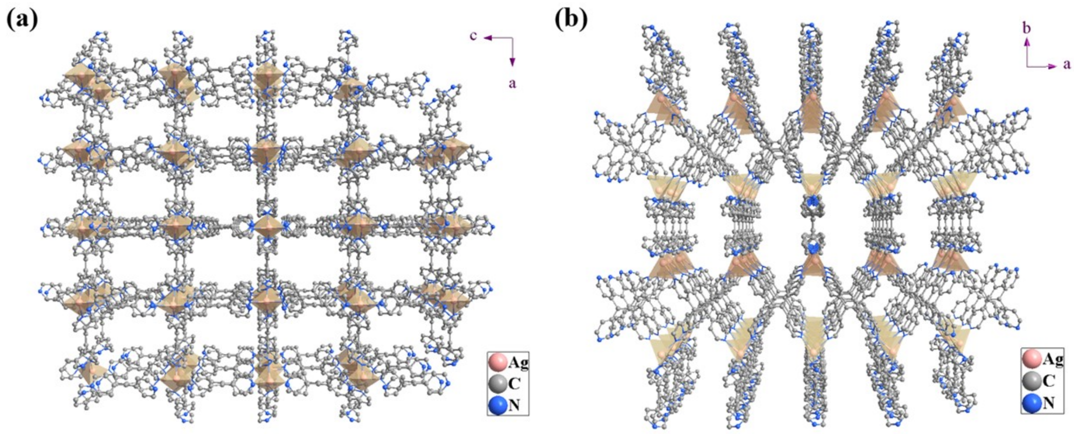

Figure S4. 3D packing structures for **1** along the *b*-axis (a) and *c*-axis (b) directions. The anionic guests are omitted for clarity. Color code: Ag, pink; N, dark blue; C, grey.

Table S3. Dihedral angles (°) of the four adjacent pyridine ring planes for the TEPE ligand.

Dihedral angle	Plane 1&2	Plane 2&3	Plane 3&4	Plane 4&1
NC	87.04	87.04	87.04	87.04
BC	72.26	72.26	72.26	72.26
NTF	51.89	79.67	51.89	84.75
ADC	49.61	87.22	48.68	87.22

2.3 Photochromic Properties

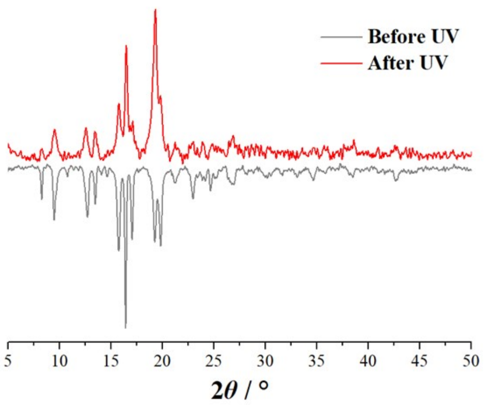

Figure S5. The PXRD patterns for 1^* (red line) at room temperature. The pattern of **1** (grey line) is shown for comparison.

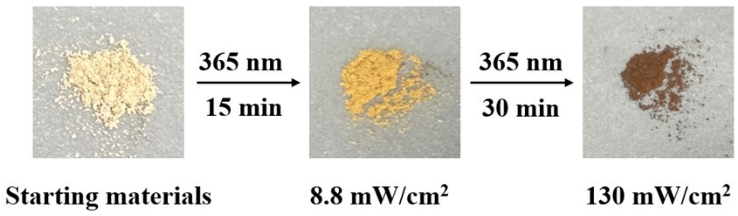

Figure. S6. The color changes of MOF **1/1*** under different power density and irradiation time of 365 nm light.

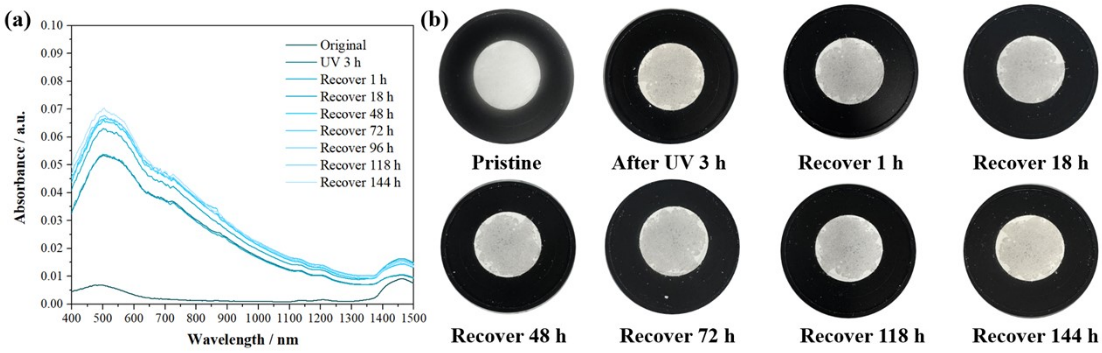

Figure. S7. (a) Time-dependent Vis-NIR diffuse reflectance spectra of the **1*** placed in the dark. (b) Images of the **1*** samples at different placement times.

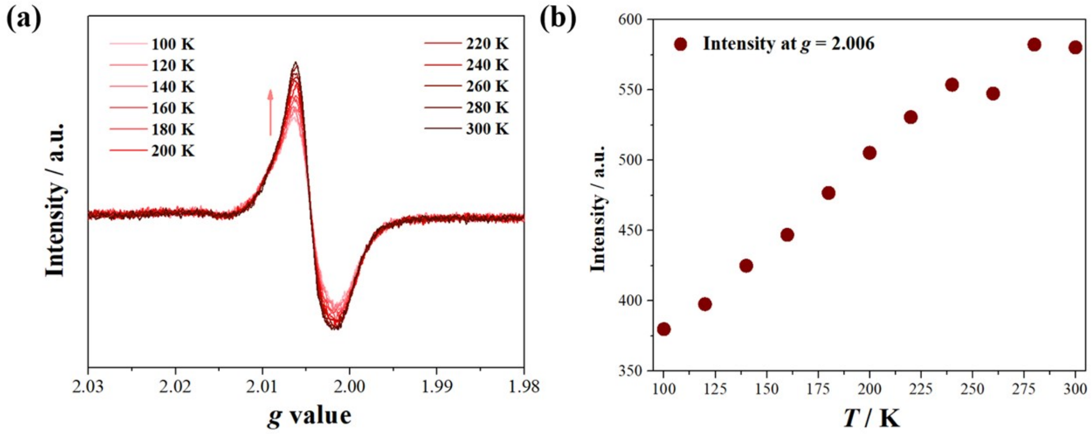

Figure S8. (a) The *g* values of variable-temperature EPR spectra for photoproduct **1***. (b) The variations of EPR intensities from 100 K to 300 K.

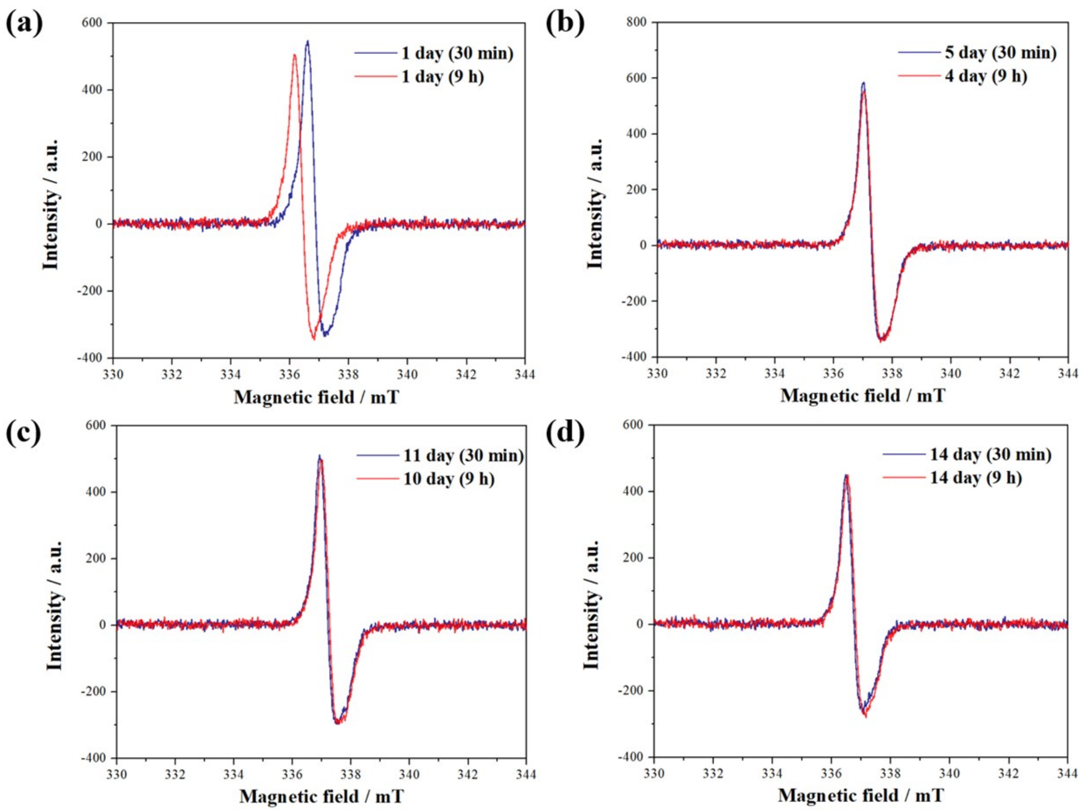

Figure S9. EPR spectra of **1*** (blue line) illuminated for 30 min and **1*** illuminated for 9 h (red line) were placed in the air atmosphere for 1 day (a), 5 (and 4) days (b), 11 (and 10) days (c) and 14 days (d). The position deviation in (a) is caused by measurement error, and the *g* values of the two samples are consistent.

2.4 Photoluminescence Performance

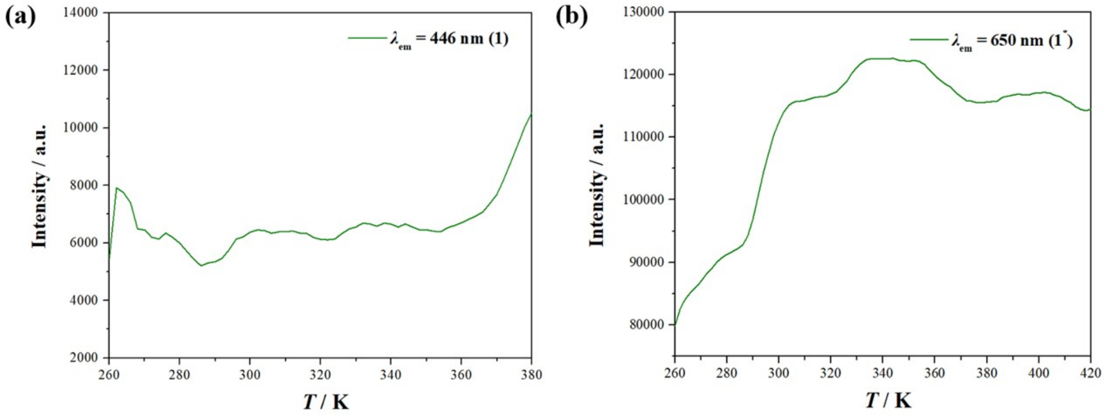

Figure. S10. (a) The room-temperature solid-state excitation spectrum of **1** (λ_{em} = 446 nm). (b) (a) The room-temperature solid-state excitation spectrum of **1*** (λ_{em} = 650 nm).

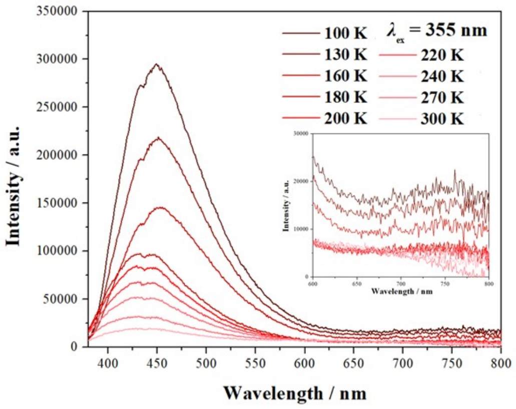

Figure S11. Temperature-dependent emission spectra of **1** (excited at 355 nm) in solid state from 100 K to 300 K. Inset shows the photoluminesence behaviors between 600 and 800 nm.

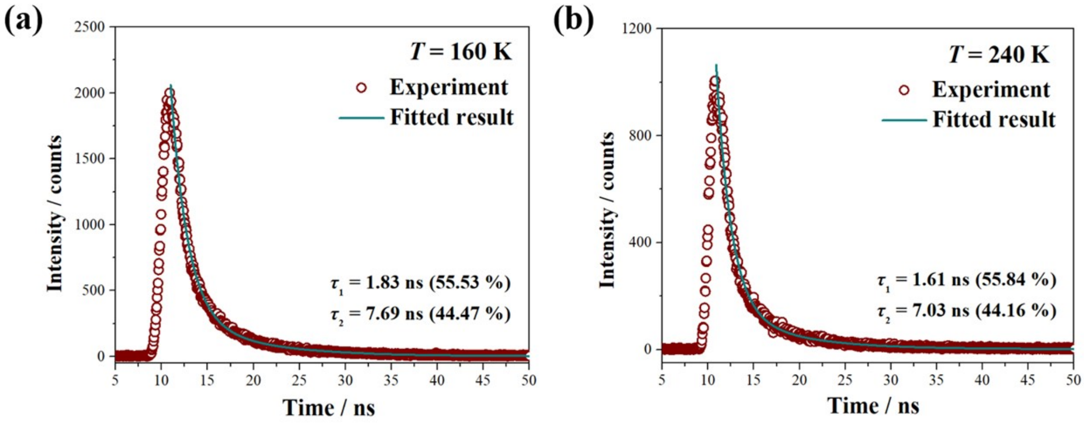

Figure S12. (a) Lifetime measurements for **1** in solid state at 160 K, with mean lifetime 55.53% τ_1 = 1.83 ns and 44.47% τ_2 = 7.69 ns fitted by a double exponential function (λ_{em} = 405 nm, λ_{em} = 450 nm). (b) Lifetime measurements for **1** in solid state at 240 K, with mean lifetime 55.84% τ_1 = 1.61 ns and 44.16% τ_2 = 7.03 ns fitted by a double exponential function (λ_{ex} = 405 nm, λ_{em} = 450 nm).

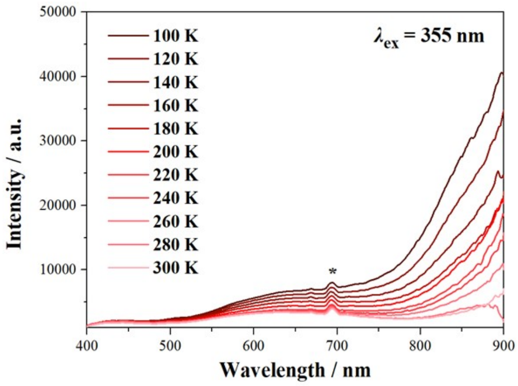

Figure S13. Temperature-dependent emission spectra of **1*** (excited at 355 nm) in solid state from 100 K to 300 K The position of the asterisk marks in the picture is due to stray light from the fluorescence spectroscopic instrument.

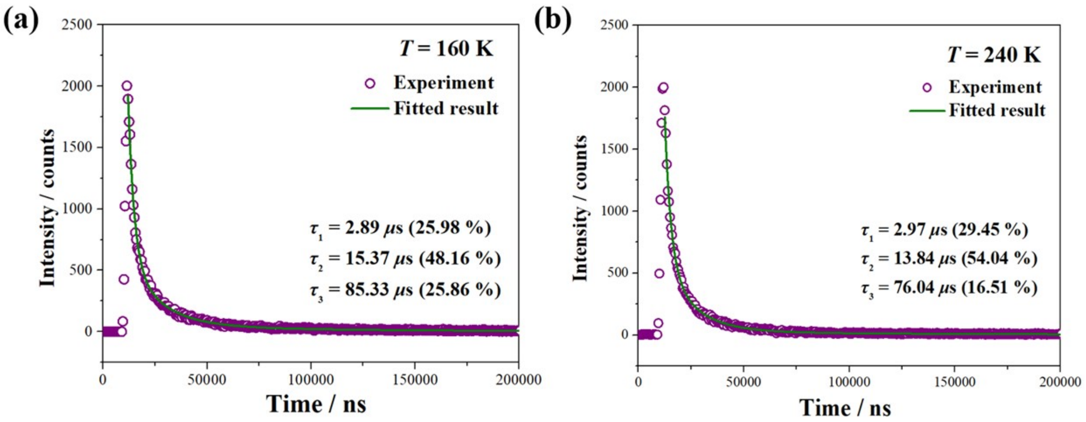

Figure S14. (a) Lifetime measurements for **1*** in solid state at 160 K, with mean lifetime 25.98% $\tau_1 = 2.89$ μs, 48.16% $\tau_2 = 15.37$ μs and 25.86% $\tau_3 = 85.33$ μs fitted by a triple exponential function (λ_{ex} = 355 nm, λ_{em} = 850 nm). (b) Lifetime measurements for **1*** in solid state at 240 K, with mean lifetime 29.45% $\tau_1 = 2.97$ μs, 54.04% $\tau_2 =13.84$ μs and 16.51% $\tau_3 = 76.04$ μs fitted by a triple exponential function (λ_{ex} = 355 nm, λ_{em} = 850 nm).

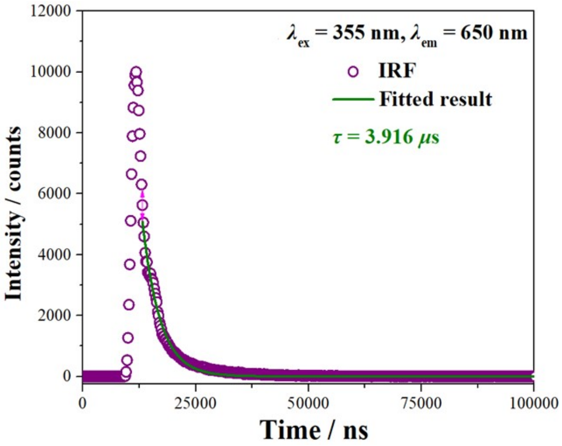

Figure S15. The interferon regulatory factor (IRF) was collected and fitted by the first-order exponential decay curve. The lifetime of the background brought by the instrument is 3.916 μs.

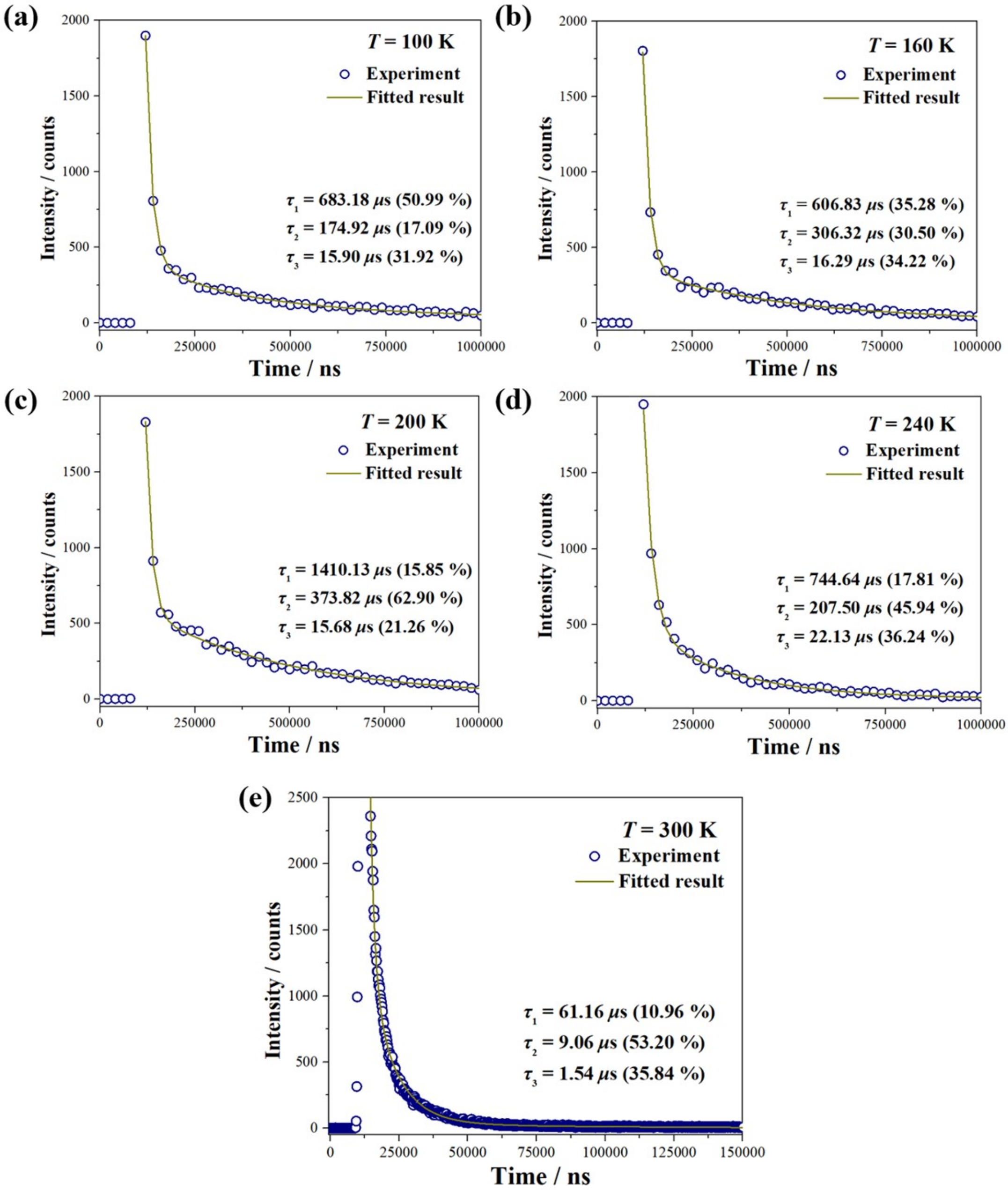

Figure S16. The lifetime measurements of **1** were measured in solid state at 100 K (a), 160 K (b), 200 K (c), 240 K (d), and 300 K (e) under 355 nm excitation monitored at 650 nm emission wavelength.

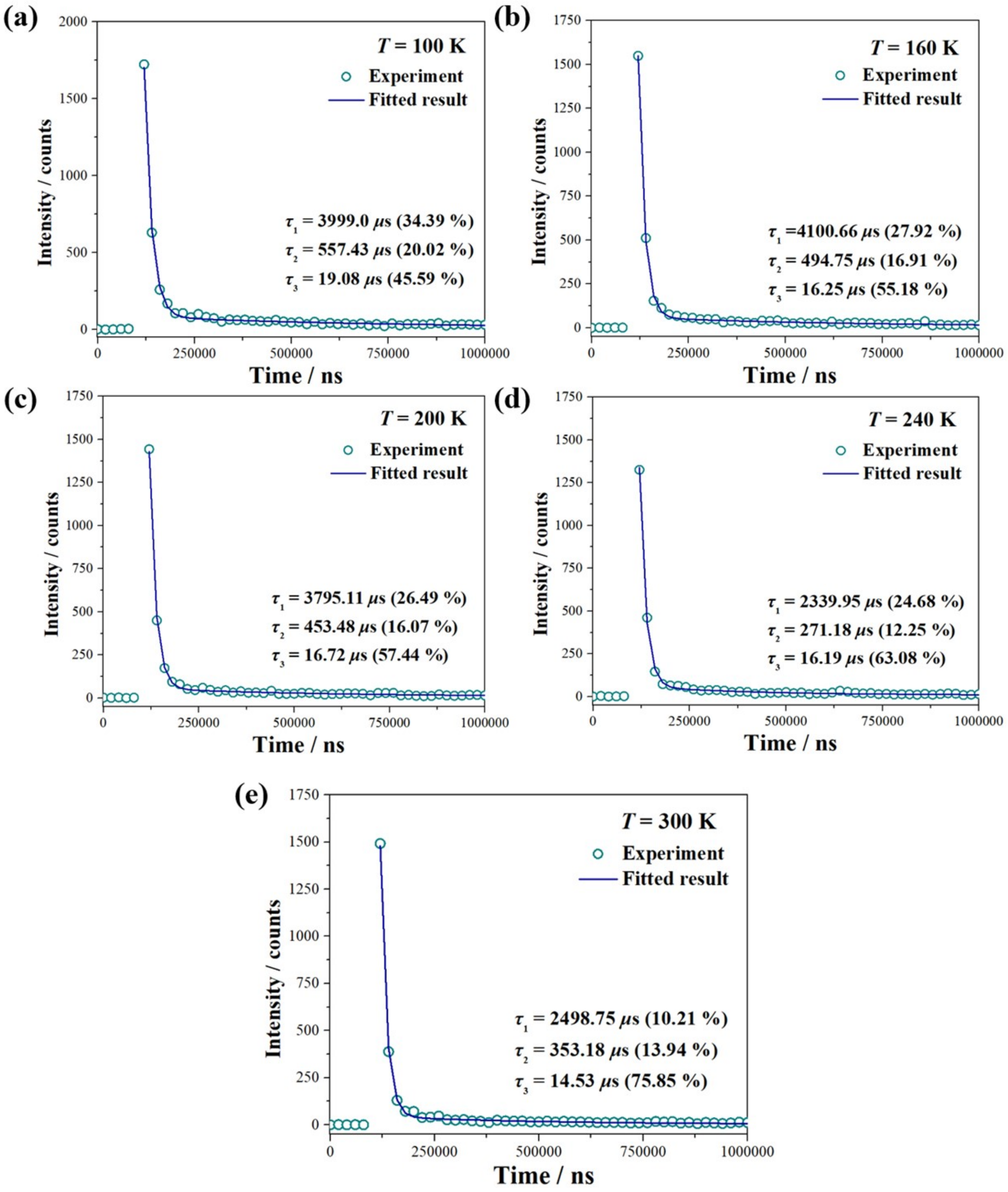

Figure S17. The lifetime measurements of **1*** were measured in solid state at 100 K (a), 160 K (b), 200 K (c), 240 K (d), and 300 K (e) under 355 nm excitation monitored at 650 nm emission wavelength.

Table S4. Lifetime measurements for **1** under the excitation of 405 nm in solid state at different temperatures (λ_{em} = 450 nm).

***T* / K**	τ_1 / ns	τ_2 / ns	τ_3 / ns
100	1.56 (53%)	7.00 (47%)	
160	1.83 (56%)	7.69 (44%)	
240	1.61 (55%)	7.03 (44%)	
300	1.12 (39%)	3.81 (45%)	12.38 (16%)

Table S5. Lifetime measurements for **1*** under the excitation of 355 nm in solid state at different temperatures (λ_{em} = 850 nm).

***T* / K**	τ_1 / μs	τ_2 / μs	τ_3 / μs
100	4.65 (18%)	12.28 (50%)	111.69 (32%)
160	2.89 (26%)	15.37 (48%)	85.33 (26%)
240	2.97 (30%)	13.84 (54%)	76.04 (16%)
300	2.52 (41%)	11.28 (51%)	49.06 (8%)

Table S6. Lifetime measurements for **1*** under the excitation of 355 nm in solid state at different temperatures (λ_{em} = 650 nm).

***T* / K**	τ_3 / μs	τ_2 / μs	τ_1 / μs
100	15.90 (32%)	174.92 (17%)	683.18 (51%)
160	16.29 (56%)	306.32 (44%)	606.83 (35%)
200	15.68 (21%)	373.82 (63%)	1410.13 (16%)
240	22.13 (36%)	207.50 (46%)	744.64 (18%)
300	1.54 (56%)	9.06 (53%)	61.16 (11%)

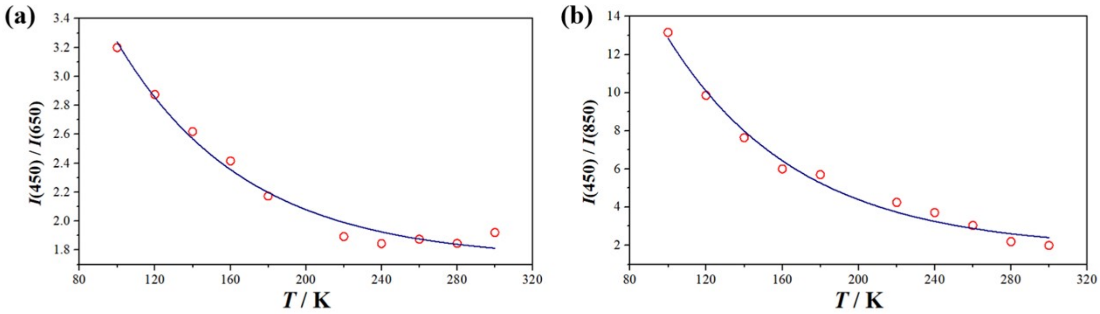

Figure. S18. The variation of the emission intensity ratio at 450 nm and 650 nm (a) and 850 nm (b) with different temperatures. The blue solid lines are the fitting results of the first-order decay exponential function (FIR function).

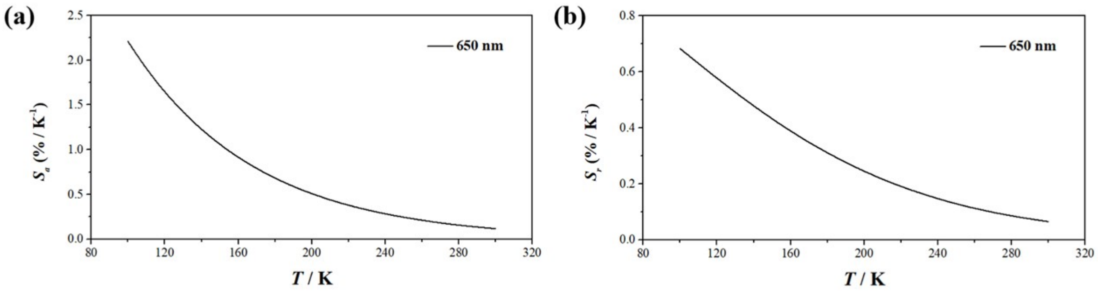

Figure. S19. The S_a (a) and S_r (b) functions of **1*** at the 650 nm.

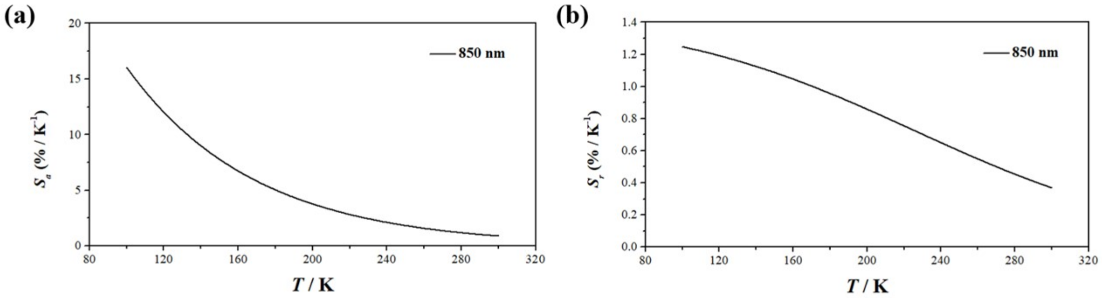

Figure. S20. The S_a (a) and S_r (b) functions of **1*** at the 850 nm.

2.5 Photothermal Conversion

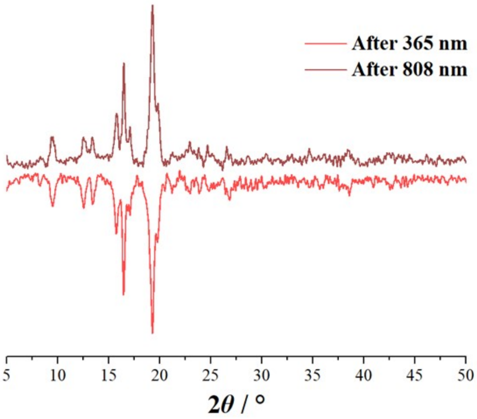

Figure S21. The PXRD patterns for **1*** (brown line) after 808 nm laser irradiation. The pattern of **1*** (red line) is shown for comparison.

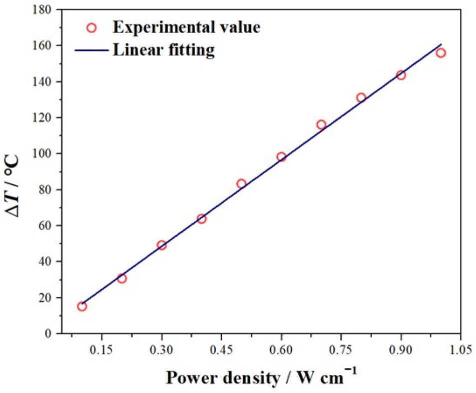

Figure S22. Plot of the average temperature increase (ΔT) of **1*** *vs.* the power density of 808 nm laser.

Photothermal conversion efficiency (*PCE*)

The photothermal conversion efficiency of **1*** was determined according to a previously established method. In detail, 3.5 mg **1*** powder was dispersed in 4 mL of pure water to form suspension at room temperature (22.5 °C). The suspension was irradiated by 0.5 W 808 nm laser for 25 min. Then, the laser was turn off and the system was allowed to cool down to room temperature naturally. During the test, the temperature of the system was recorded by an IR camera.

The ***PCE*** can be calculated by **Equation S1**

$$PCE = \frac{hs(\Delta T_{material} - \Delta T_{solvent})}{I(1 - 10^{-A})}$$

Equation S1

Herein, I is the laser power (0.5 W); A is the absorbance of the suspension at the wavelength of 808 nm. $\Delta T_{material}$ and $\Delta T_{solvent}$ was the temperature changes of the suspension and blank solvent (pure water), respectively. h is the heat transfer coefficient and s is the surface area of the container, which were determined by **Equation S2**

$$hs = \frac{mc}{\tau_s}$$

Equation S2

In **Equation S2**, m is the mass of the solvent (4 × 1.0 = 4.0 g, as density of pure water is 1.0 g mL^{-1}); c is the specific heat capacity of the solvent (4.18 J g^{-1} K^{-1} for water); and τ_s is a time constant, which can be determined from the cooling periods according to **Equation S3**

$$t = -\tau_s \ln(\theta)$$

Equation S3

θ is the driving force temperature defined by **Equation S4**

$$\theta = \frac{T - T_{Surr}}{T_{Max} - T_{Surr}}$$

Equation S4

T_{Max} (30.2 °C) and T_{Surr} (22.5 °C) were the maximum steady-state temperature and the environmental temperature, respectively.
The ***PCE*** value of **1*** at 808 nm wavelength was calculated as follow—

$hs = 4.0 \times 4.18 / 784.2 = 0.02132$

$\Delta T_{material} - \Delta T_{solvent} = 6.6$ °C

I was 0.5 W and ***A*** was 0.425.

Thus, according to **Equation S1**, ***PCE*** was $0.02132 \times 6.6 / [0.5 \times (1 - 10^{-0.425})] = 45.09\%$ under the 808 nm irradiation.

Solar−driven water evaporation

20 mg of powdery **1*** was ultrasonically dispersed in 2 mL of water. A piece of air laid paper (rectangle) was placed on a round foam. Two slits was cut throug the round foam so that the air laid paper could cross through the foam to reach the undersurface to draw water by capillary forces. The remaining part of air laid paper on the upper surface was a square with length of 2.0 cm.The **1*** suspensions was droped onto the square airlaid paper. The round foam with **1***-loaded airlaid paper was put on a culture petri dish filled with water. The whole system was surrounded by thermally insulating foam.

Simulated sunlight was gengerated by a 500 W Xenon lamp (CEL-S500-T5) equipped with an AM 1.5 G optical filter. The optical intensity was corrected to 1000 W m^{-2} (1 sun) by the photometer. This simulated sunlight was used to irradiate the above−mentioned system vertically. The mass change of the water was recorded by an electronic analytical balance (accuracy of 0.00001 g). The IR thermal camera was used to measure the temperature. All experiments were conducted at an ambient temperature of 20 °C with a humidity of 67%.

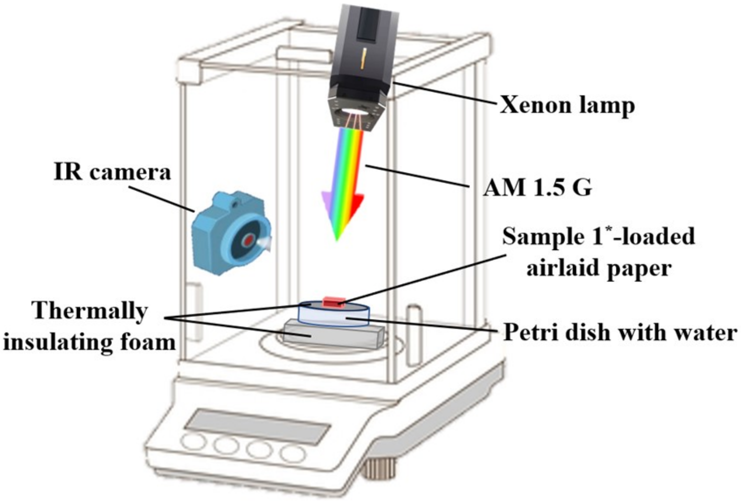

Figure S23. Schematic diagram of solar-driven water evaporation experiments.

Calculation of the efficiency of solar−driven water evaporation

The efficiency ($\boldsymbol{\eta}$) was calculated[9] based on the following equation:

$$\eta = \frac{mh_{LV}}{tP_0}$$

Equation S5

where $\boldsymbol{m}$ refers to the mass flux (evaporation rate under 1 sun illumination minus the rate in dark environment) of water, $\boldsymbol{h_{LV}}$ refers to the total liquid−vapor phase−change enthalpy (i.e., the sensible heat and the enthalpy of evaporation $\boldsymbol{h_{LV} = Q + \Delta h_{vap}}$), $\boldsymbol{Q}$ is the energy consumption to heat the system from the initial temperature $\boldsymbol{T_0}$ to the final temperature $\boldsymbol{T}$, $\boldsymbol{\Delta h_{vap}}$ is the latent heat of evaporation of water. And $\boldsymbol{t}$ is the normalized irradiation time (3600 s), $\boldsymbol{P_0}$ is the normalized solar irradiation intensity, 1000 W m^{-2}.

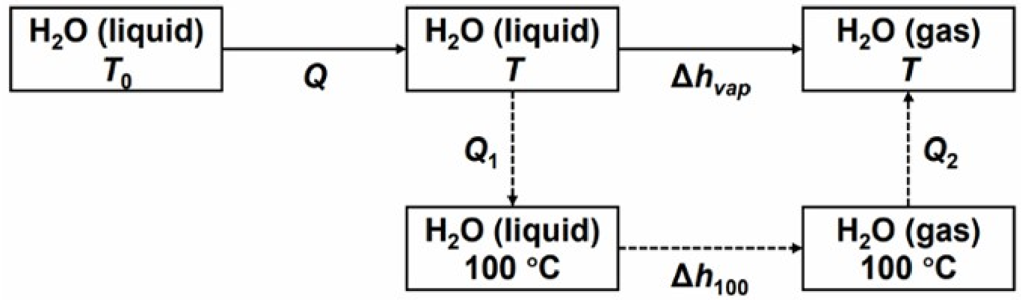

$\boldsymbol{Q} = c_{liquid} \times (\boldsymbol{T} - \boldsymbol{T_0})$

$\boldsymbol{\Delta h_{vap}} = \boldsymbol{Q_1} + \Delta \boldsymbol{h_{100}} + \boldsymbol{Q_2}$

$\boldsymbol{Q_1} = c_{liquid} \times (100\ ^{o}\mathrm{C} - \boldsymbol{T})$

$\boldsymbol{Q_2} = c_{vapor} \times (\boldsymbol{T} - 100\ ^{o}\mathrm{C})$

In our experiments, c_{liquid}, the specific heat capacity of water is a constant of 4.18 J g^{-1} ^{o}C^{-1}. c_{vapor}, the specific heat capacity of vapor is a constant of 1.865 J g^{-1} ^{o}C^{-1}. $\boldsymbol{\Delta h_{100}}$ is the latent heat of evaporation of water at 100 ^{o}C, taken to be 2260 kJ kg^{-1}.

The surface temperature of **1***-loaded airlaid paper was 37.2 ^{o}C during the evaporation process, therefore $\boldsymbol{T}$ is 37.2 ^{o}C. As the aforementioned equations,

$\boldsymbol{Q} = c_{liquid} \times (\boldsymbol{T} - \boldsymbol{T_0}) = 4.18 \times (37.2 - 20.4) = 70.224$ kJ kg^{-1}

$\boldsymbol{\Delta h_{vap}} = \boldsymbol{Q_1} + \boldsymbol{\Delta h_{100}} + \boldsymbol{Q}$

$= 4.18 \times (100 - 37.2) + 2260 + 1.865 \times (37.2 - 100)$ kJ kg^{-1}

$= 2405.382$ kJ kg^{-1}

$\Delta \boldsymbol{h_{LV}} = \boldsymbol{Q} + \boldsymbol{\Delta h_{vap}}$

$= 70.224 + 2405.382$ kJ kg^{-1}

$= 2475.606$ kJ kg^{-1}

$\boldsymbol{m} = 1.202 - 0.0384 = 1.164$ kg m^{-2} h^{-1}

$\boldsymbol{t} = 3600$ s

$\boldsymbol{P_0} = 1000$ W m^{-2}

As a result, evaporation efficiency $\boldsymbol{\eta} = \boldsymbol{mh_{LV}/tP_0} = 80.0\%$.

2.6 Computational Details

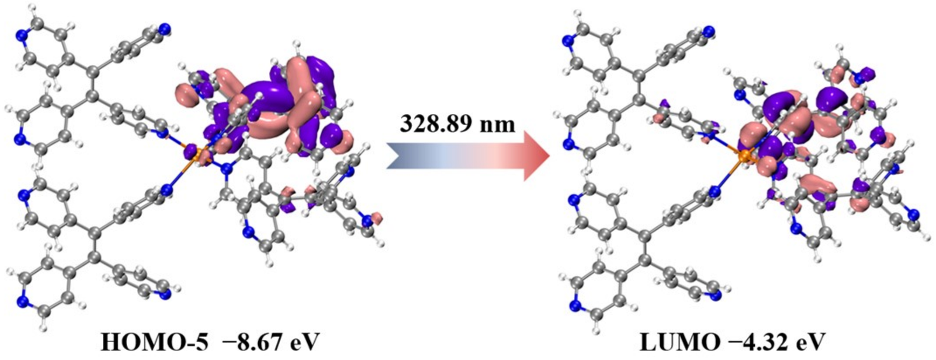

Figure S24. Pictorial representation of the transition from HOMO-5 to LUMO orbitals of **1** at the absorbance of 328.89 nm.

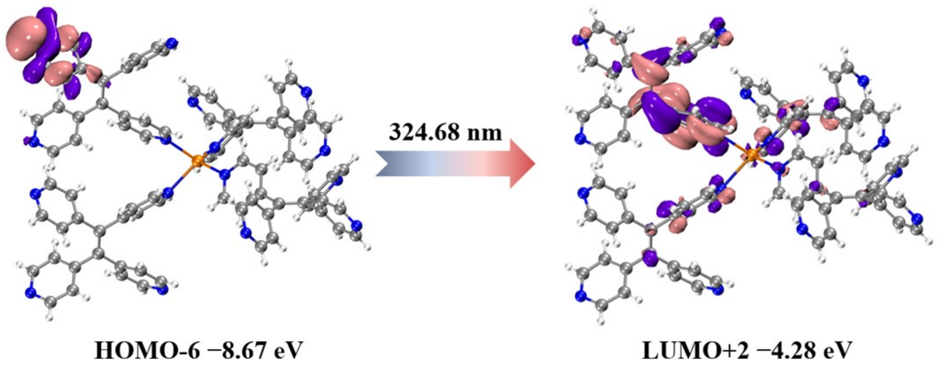

Figure S25. Pictorial representation of the transition from HOMO-6 to LUMO+2 orbitals of **1** at the absorbance of 324.68 nm.

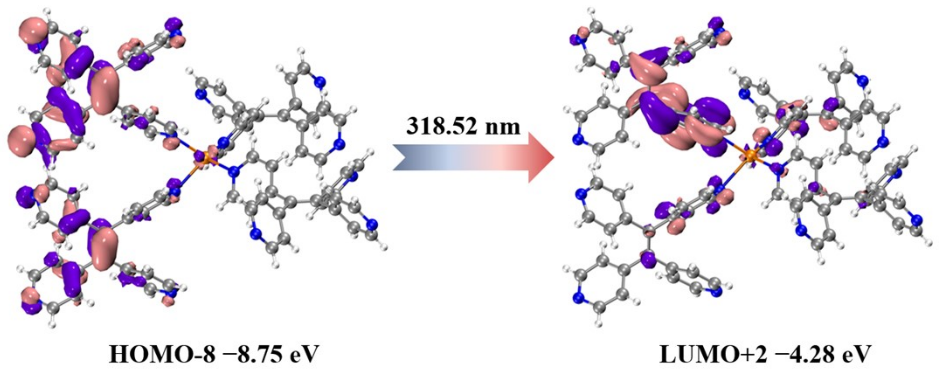

Figure S26. Pictorial representation of the transition from HOMO-8 to LUMO+2 orbitals of **1** at the absorbance of 318.52 nm.

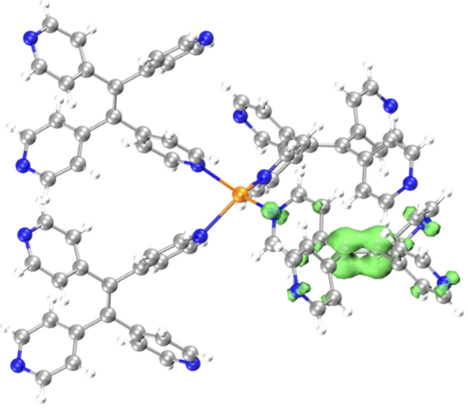

Figure S27. The calculated spin density distribution of the triplet state **1***, with a spin density isovalue of 0.01.

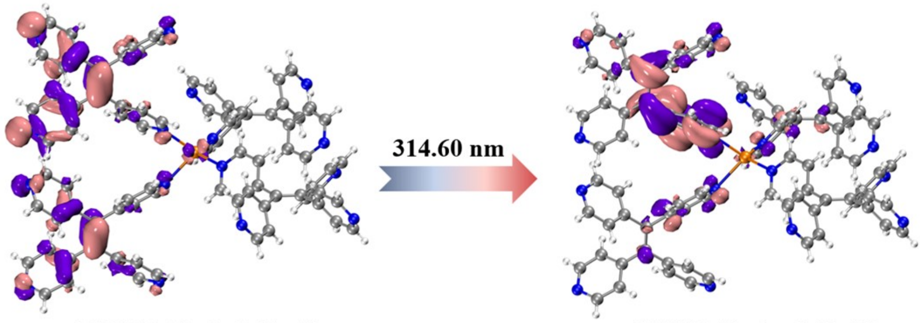

HOMO(β)-6 −8.71 eV **LUMO(β)+2 −4.22 eV**

Figure S28. Pictorial representation of the transition from HOMO-6 to LUMO+2 orbitals of **1*** at the absorbance of 314.60 nm.

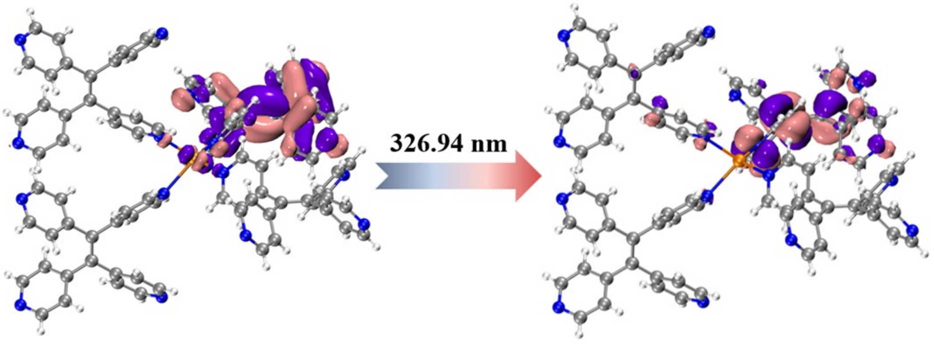

HOMO(α)-4 −8.62 eV **LUMO(α) −4.26 eV**

Figure S29. Pictorial representation of the transition from HOMO-6 to LUMO+2 orbitals of **1*** at the absorbance of 326.94 nm.

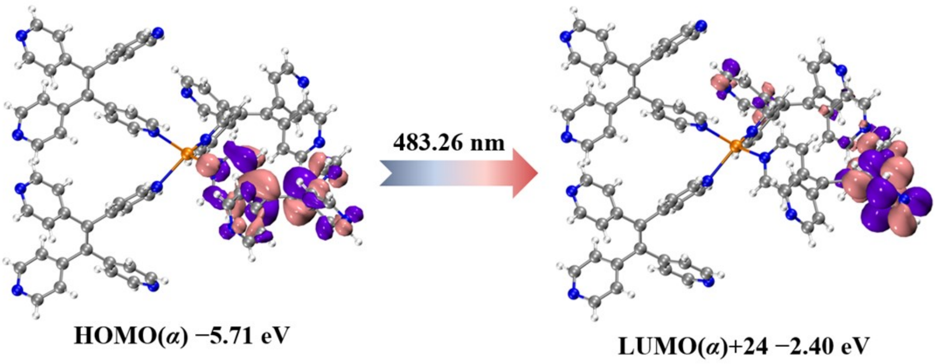

Figure S30. Pictorial representation of the transition from HOMO-6 to LUMO+2 orbitals of **1*** at the absorbance of 483.26 nm.

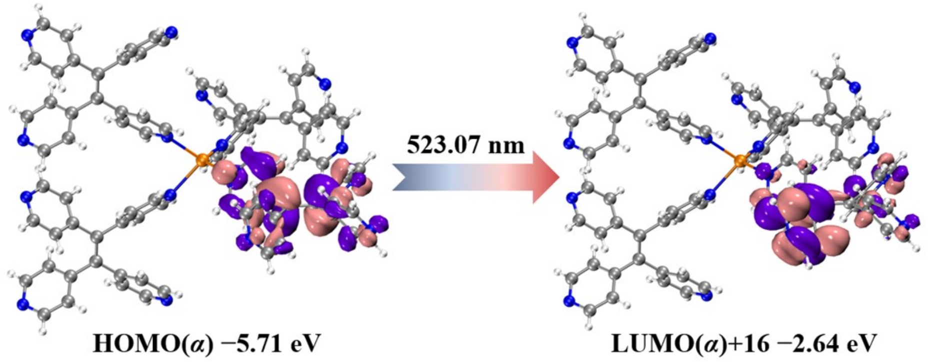

Figure S31. Pictorial representation of the transition from HOMO to LUMO+16 orbitals of **1*** at the absorbance of 523.07 nm.

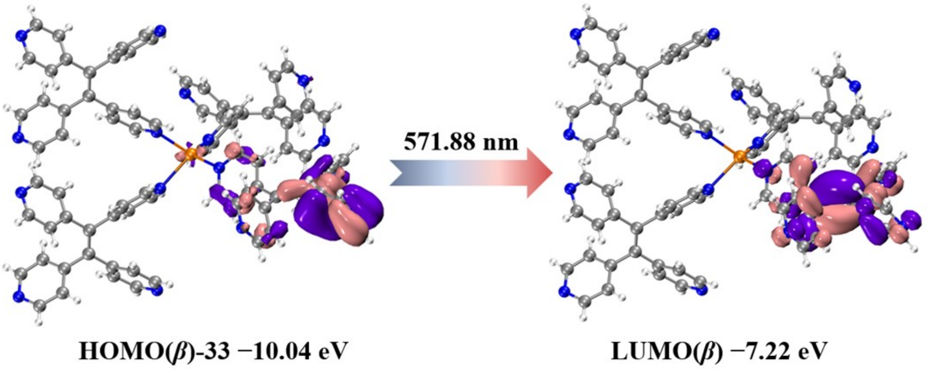

Figure S32. Pictorial representation of the transition from HOMO-33 to LUMO orbitals of **1*** at the absorbance of 571.88 nm.

Reference

[1] G. M. Sheldrick, *Acta Crystallogr. Sect. A Found. Crystallogr.* **2015**, *71*, 3–8.

[2] O. V. Dolomanov, L. J. Bourhis, R. J. Gildea, J. A. K. Howard, H. Puschmann, *J. Appl. Crystallogr.* **2009**, *42*, 339–341.

[3] G. M. Sheldrick, *Acta Crystallogr. Sect. C Struct. Chem.* **2015**, *71*, 3–8.

[4] P. van der Sluis, A. L. Spek, *Acta Crystallogr. Sect. A Found. Crystallogr.* **1990**, *46*, 194–201.

[5] Grimme, S.; Antony, J.; Ehrlich, S.; Krieg, H. *J. Chem. Phys.* **2010**, *132* (15), 154104.

[6] M. J. Frisch, G. W. Trucks, H. B. Schlegel, G. E. Scuseria, M. A. Robb, J. R. Cheeseman, G. Scalmani, V. Barone, B. Mennucci, G. A. Petersson, H. Nakatsuji, M. Caricato, X. Li, H. P. Hratchian, A. F. Izmaylov, J. Bloino, G. Zheng, J. L. Sonnenberg, M. Hada, M. Ehara, K. Toyota, R. Fukuda, J. Hasegawa, M. Ishida, T. Nakajima, Y. Honda, O. Kitao, H. Nakai, T. Vreven, J. A. Montgomery, Jr., J. E. Peralta, F. Ogliaro, M. Bearpark, J. J. Heyd, E. Brothers, K. N. Kudin, V. N. Staroverov, T. Keith, R. Kobayashi, J. Normand, K. Raghavachari, A. Rendell, J. C. Burant, S. S. Iyengar, J. Tomasi, M. Cossi, N. Rega, J. M. Millam, M. Klene, J. E. Knox, J. B. Cross, V. Bakken, C. Adamo, J. Jaramillo, R. Gomperts, R. E. Stratmann, O. Yazyev, A. J. Austin, R. Cammi, C. Pomelli, J. W. Ochterski, R. L. Martin, K. Morokuma, V. G. Zakrzewski, G. A. Voth, P. Salvador, J. J. Dannenberg, S. Dapprich, A. D. Daniels, O. Farkas, J. B. Foresman, J. V. Ortiz, J. Cioslowski, and D. J. Fox, Gaussian, Inc., Wallingford CT, 2013; Gaussian 16, Revision A.03, M. J. Frisch, G. W. Trucks, H. B. Schlegel, G. E. Scuseria, M. A. Robb, J. R. Cheeseman, G. Scalmani, V. Barone, G. A. Petersson, H. Nakatsuji, X. Li, M. Caricato, A. V. Marenich, J. Bloino, B. G. Janesko, R. Gomperts, B. Mennucci, H. P. Hratchian, J. V. Ortiz, A. F. Izmaylov, J. L. Sonnenberg, D. Williams-Young, F. Ding, F. Lipparini, F. Egidi, J. Goings, B. Peng, A. Petrone, T. Henderson, D. Ranasinghe, V. G. Zakrzewski, J. Gao, N. Rega, G. Zheng, W. Liang, M. Hada, M. Ehara, K. Toyota, R. Fukuda, J. Hasegawa, M. Ishida, T. Nakajima, Y. Honda, O. Kitao, H. Nakai, T. Vreven, K. Throssell, J. A. Montgomery, Jr., J. E. Peralta, F. Ogliaro, M. J. Bearpark, J. J. Heyd, E. N. Brothers, K. N. Kudin, V. N. Staroverov, T. A. Keith, R. Kobayashi, J. Normand, K. Raghavachari, A. P. Rendell, J. C. Burant, S. S. Iyengar, J. Tomasi, M. Cossi, J. M. Millam, M. Klene, C. Adamo, R. Cammi, J. W. Ochterski, R. L. Martin, K. Morokuma, O. Farkas, J. B. Foresman, and D. J. Fox, Gaussian, Inc., Wallingford CT, **2016**.

[7] Lu, T.; Chen, F. *J. Comput. Chem.* **2012**, *33* (5), 580–592.

[8] Humphrey, W.; Dalke, A.; Schulten, K. *J. Mol. Graph.* **1996**, *14*, 33–38.

[9] Y. Su, Z. Chen, X. Tang, H. Xu, Y. Zhang, C. Gu, *Angew. Chem. Int. Ed.* **2021**, *60*, 24424 – 24429.